Matter, Volume *2*

Supplemental Information

Disturbance-Promoted Unconventional and Rapid Fabrication of Self-Healable Noble Metal Gels for (Photo-)Electrocatalysis

Ran Du, Jan-Ole Joswig, Xuelin Fan, René Hübner, Daniel Spittel, Yue Hu, and Alexander Eychmüller

Experimental Procedures

Reagents and Materials

Reagents including hydrogen tetrachloroaurate (III) ($HAuCl_4 \cdot 3H_2O$), silver nitrate ($AgNO_3$), potassium tetrachloropalladate (II) (K_2PdCl_4), potassium tetrachloroplatinate (II) (K_2PtCl_4), ammonium hexachlororhodate (III) ($(NH_4)_3RhCl_6$), trisodium citrate dihydrate (NaCA), sodium borohydride ($NaBH_4$), polyvinylpyrrolidone (PVP, M_w = 58000), 20% palladium on carbon, and others were purchased from Sigma-Aldrich or Alfa-Aesar. All reagents are used without further purification.

Fabrication of Noble Metal Hydrogels (NMHs)

Hydrogels were synthesized by either a one-step method or a two-step method at ambient temperature (~293 K), which is started from a metal salt solution or a metal nanoparticle (NP) solution. Multimetallic hydrogels were synthesized via a similar route to that for single-metal hydrogels, except that several metal precursor salts were mixed at an equal molar ratio before further reduction and initiation. In comparison to previous reports, after initiation with specific additives (e.g. NH_4F), a prolonged stirring time (1–5 min) or other disturbing approaches were applied for accelerating the gelation process.

One-step method

The fabrication process of a $NaBH_4$-triggered one-step gelation of gold salt solutions is described as an example. Under stirring (e.g., 600 rpm), an aqueous solution of $HAuCl_4 \cdot 3H_2O$ (32.5 mM, 30.8 μL) was added to water (4.87 mL), followed by the addition of freshly prepared $NaBH_4$ aqueous solution (1.0 M, 100.0 μL). After continuously stirring for *ca.* 90 s, the resulting gel pieces were manually assembled together to form a monolithic gel. For the experiments where ligands were included, an aqueous solution of the corresponding ligand (400.0 mM, 25.0 μL) was added before adding the gold salts. The fabrication process can be scaled up to 800 mL, where the stirring time was set to 3–5 min and the settling/assembling time was set to *ca.* 10 min.

Two-step method

The two-step method is divided into two processes, i.e. the nanoparticle preparation and the hydrogel formation. The process of NH_4F-triggered gelation of NaCA-stabilized gold NP solutions is described here as an example.

Preparation of the Gold Nanoparticle Solution

Aqueous solutions of NaCA (400 mM, 25.0 μL) and $HAuCl_4 \cdot 3H_2O$ (32.5 mM, 30.8 μL) were added successively to 4.88 mL water and stirred for ~2 min. Then freshly prepared $NaBH_4$ aqueous solution (200 mM, 20.0 μL) was rapidly injected, followed by stirring for ca. 2 min. The molar ratio of the metal salt (M), ligand (L), and reductant (R) was fixed at 1 / 10 / 4.

Preparation of the Gold Hydrogel

An aqueous solution of NH_4F (10.0 M, 50 μL) was added to the as-prepared gold NP solution (4.95 mL). After continuously stirring for *ca.* 90 s, the resulting gel pieces were manually assembled together to form a monolithic gel. The fabrication process can be scaled up to 800 mL by using similar procedures.

Dynamic shelling approach (DSA)

Aqueous solutions of NaCA (400 mM, 62.5 μL) and $HAuCl_4 \cdot 3H_2O$ (32.5 mM, 38.5 μL) were added successively to 4.76 mL water under stirring at 600 rpm. Then freshly prepared $NaBH_4$ aqueous solution (200 mM, 50.0 μL) and NH_4F aqueous solution (10.0 M, 50.0 μL) were successively added. After stirring for ca. 15s, an aqueous solution of K_2PtCl_4 (32.5 mM, 38.5 μL) was added. The stirring was continued for ~90 s and the resulting aggregates were manually assembled to yield the final Au-Pt core-shell-structured gel.

Fabrication of Noble Metal Aerogels (NMAs)

The as-prepared hydrogels were washed by a large amount of water for 4–5 times with a total duration of 2–3 days to remove possible residues. Later on, the hydrogels were solvent-exchanged at 303 K with tert-butanol for 2 times. Afterwards, the resulting wet gels were flash-freezed by liquid nitrogen and remained at -196 ºC for ~10 min to enable complete freezing. The frozen samples were put into the chamber of a freeze dryer (TOPTI-12S-80), performing the drying process at ~1 Pa for 12–24 h, where the temperature of the cold trap was set to -80 ºC. The yield of NMAs was calculated based on the mass of the final aerogels with reference to the mass of the corresponding precursor metal salts.

Computational Procedures

Monte–Carlo (MC) simulations

A self-developed random walk Monte-Carlo algorithm was used for simulating the influence of disturbances on the gelation process. The initial positions of particles (the radius is arbitrarily fixed to 3 nm) were generated randomly in a spherical space with a volume of 2.1×10^6 nm^3. All particles were non-interacting. In each Monte-Carlo step, all particles (or aggregates) were either moved translationally or rotated (both with a probability of 50%). If – during translation or rotation – two particles (or aggregates) met, they were considered as one aggregate afterwards. The algorithm was terminated if all particles were aggregated to one single rigid aggregate. Translational movements were performed with a randomly chosen step length (between 0 nm and the maximum step length x, x = 1 nm, 2 nm, and 3 nm). Rotations were performed with a randomly chosen rotation angle (between 0° and 10°).

For the calculation of radius of gyration (R_g), all single particles were neglected (for point-like particles, R_g = 0), and only aggregates (with 2 or more particles) were considered. For the calculation of R_g from a not fully aggregated system (consisting of 2 or more aggregates), the radius of gyration is averaged over all aggregates. The radius of gyration of a single aggregate is calculated as:

$$R_g = \sqrt{\lambda_x^2 + \lambda_y^2 + \lambda_z^2}$$

where λ_x^2, λ_y^2, λ_z^2 are the eigenvalues of the diagonalized radius-of-gyration tensor of the n-particle aggregate:

$$G = \frac{1}{n}\sum_{i=1}^{n}\begin{pmatrix} x_i x_i & x_i y_i & x_i z_i \\ y_i x_i & y_i y_i & y_i z_i \\ z_i x_i & z_i y_i & z_i z_i \end{pmatrix}$$

For each parameter set, 1000 MC runs were performed for statistical analysis.

Characterizations

Microscopy Characterization

Scanning electron microscopy (SEM) analysis was performed on a Zeiss Gemini 500 or a Nova 200 NanoSEM scanning electron microscope. Samples were prepared by directly sticking on conductive tape.

Transmission electron microscopy (TEM) analysis was carried out by using a FEI Tecnai G2 20 or a JEM-2100F microscope operated at 200 kV. Samples were prepared by dispersing in acetone under ultrasonication (15 s to 120 s, depending on their dispersing ability), followed by dropping onto carbon-coated copper grids and drying at ambient temperature.

High-angle annular dark-field scanning transmission electron microscopy (HAADF-STEM) imaging and spectrum imaging based on energy-dispersive X-ray spectroscopy (EDX) were performed at 200 kV with a Talos F200X microscope equipped with an X-FEG electron source and a Super-X EDX detector system (FEI). Prior to STEM analysis, the specimen mounted in a high-visibility low-background holder was placed for 2 s into a Model 1020 Plasma Cleaner (Fischione) to remove possible contamination.

Optical imaging was performed on a Carl Zeiss Microscopy, with the magnification of 63×10.

Diffraction Characterization

X-ray powder diffraction (XRD) was carried out in reflection mode on a Siemens D5000 X-ray diffractometer operated at a voltage of 30 kV and a current of 10 mA with Cu Kα radiation (λ = 1.5406 Å). The data were collected in the range of 20°–90° (2θ) with a step size of $\Delta 2\theta$ = 0.02°. The sample was fixed on the holder by Scotch tape. For the single-metal system, the crystallite size was estimated by the Scherrer equation applying a crystallite-shape factor K = 0.9.

Spectroscopy Characterization

Ultraviolet–visible spectroscopy (UV-vis) absorption spectra were recorded on a Cary 60 UV-Vis Spectrophotometer.

Element Analysis

X-ray photoelectron spectroscopy (XPS) was performed on an Axis Ultra spectrometer (Kratos, UK) with a high-performance Al monochromatic source operated at 15 kV. The XPS spectra were taken after all binding energies were referenced to the C 1s neutral carbon peak at 284.8 eV, and the elemental compositions were determined from the peak area ratios after correction for the sensitivity factor by CasaXPS.

Inductively coupled plasma optical emission spectroscopy (ICP-OES) was performed on a Perkin-Elmer Optima 7000DV optical emission spectrometer.

Gas Adsorption Measurement

Nitrogen adsorption experiments were performed with a Quantachrome NOVA 3000e system at 77 K. The sample was outgassed at 323 K for ~24 h under vacuum before measurement. The filling rod was used to reduce the dead volume, thus improving the measurement accuracy. The specific surface area was calculated by using the multi-point BET equation ($0.1 < p/p_0 < 0.3$). The pore size distribution was derived by using the non-local density functional theory (NLDFT) method (N_2 at 77 K on carbon) based on a slit pore geometry. The total pore volume was calculated at $p/p_0 = 0.99$, similar to the value derived by the BJH (Barret–Joyner–Halender) method. For low-surface-area samples, instead of nitrogen, krypton (Kr) was used as the probe molecule to quantify the specific surface area, due to their lower saturation pressure (≈2.63 Torr for supercooled liquid krypton at 77K) compared to that of nitrogen molecules (≈760 Torr at 77K), thus allowing to acquire a much more accurate result ascribed to a large relative pressure change with a small amount of gas adsorption/desorption.

Electrochemical Measurements

All electrochemical tests were performed with a three-electrode system on an Autolab/PGSTAT 30 (Eco Chemie B. V. Utrecht, the Netherlands) or a CHI potentiostat (CHI 760D). A glassy carbon electrode (GCE, 3 mm in diameter), an Ag/AgCl (saturated KCl aqueous solution) electrode, and a platinum foil were used as working electrode, reference electrode, and counter electrode, respectively.

For modification of the working electrode, ~1.0 mg catalyst was dispersed in 425 μL 2-propanol (IPA) and 75 μL Nafion (1 wt.% in IPA) by sonicating for ca. 30 min to acquire the catalyst ink. Then a specific amount of ink was transferred onto the GCE and evaporated at ambient temperature. The concentrations of Pd and Pt in the ink were determined by ICP-OES, and the total loading of Pd and Pt (m_{Pd+Pt}) was calculated accordingly to ~20 μg cm^{-2}.

For the electro-oxidation of ethanol, the test was performed under N_2 atmosphere in 1.0 M KOH aqueous solution containing 1.0 M ethanol. CV curves were recorded between -0.9 and 0.3 V (*vs.* AgCl/Ag) with a scanning rate of 50 mV s^{-1}. The stability test was conducted at the potential of -0.23 V (*vs.* AgCl/Ag). For the photoelectrocatalysis, a round panel with seven LED lamps (7×OSRAM SSL 80 Streetwhite on round PCB (Color: 5700–7500 K, wavelength 350–800 nm), LED. Tech. The diameter of the panel is 35 mm, white LEDs are evenly distributed on the panel) was closely placed under the electrolytic cell. The LEDs were lightened by a tunable power source. The light power density (0–133.6 mW cm^{-2}) was calibrated by taking advantage of its linear relationship with the input power (**Figure S23a**), which was derived from an optical power meter assuming an even light field distribution and neglecting the interactions between light and the electrolyte solution.

Figures

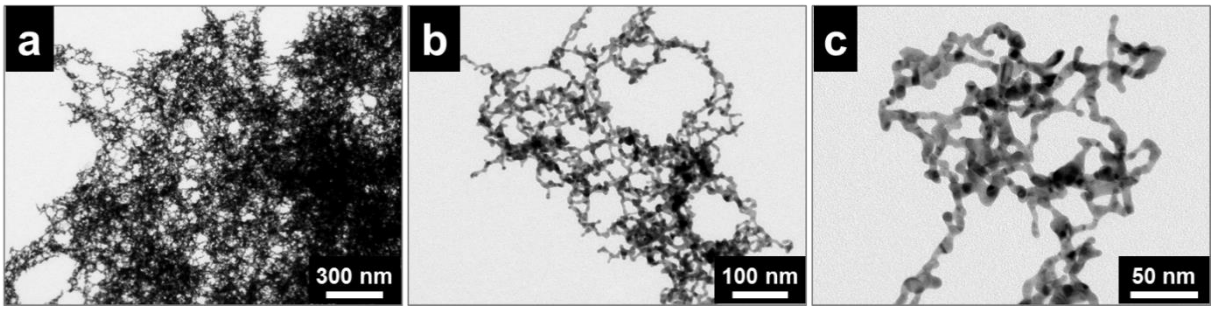

Figure S1. TEM images of gold aggregates after addition of NH_4F to NaCA-stabilized gold NP solutions (c_M = 0.2 mM) and stirring for 45 s.

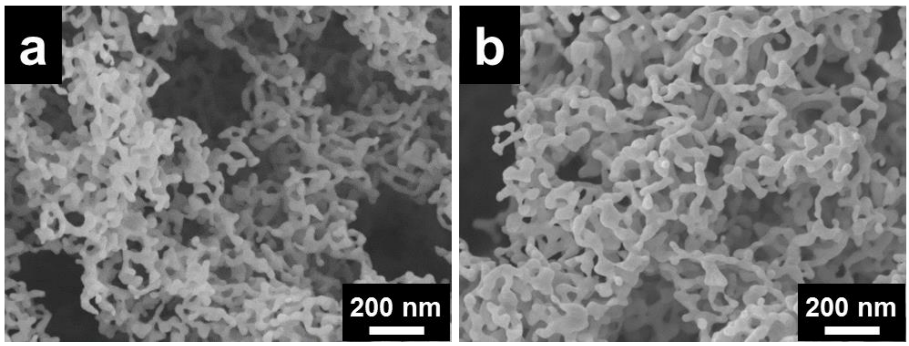

Figure S2. SEM images of gold aerogels prepared by NH_4F-induced gelation under (a) static and (b) stirring environment.

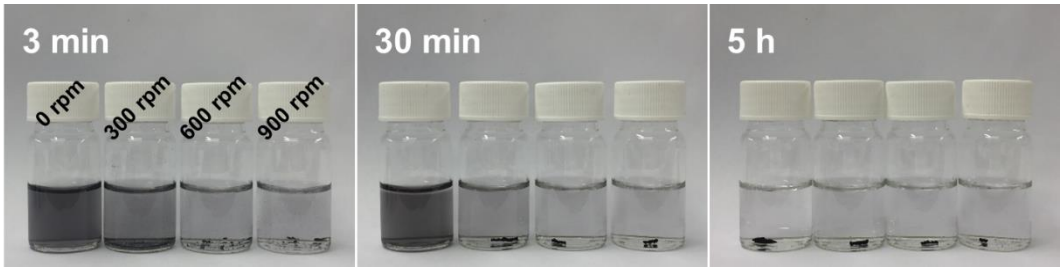

Figure S3. Time-lapse photographs of the gelation process of gold NP solutions (triggered by NH_4F) under stirring at different speed (0, 300, 600, and 900 rpm) for 2 min.

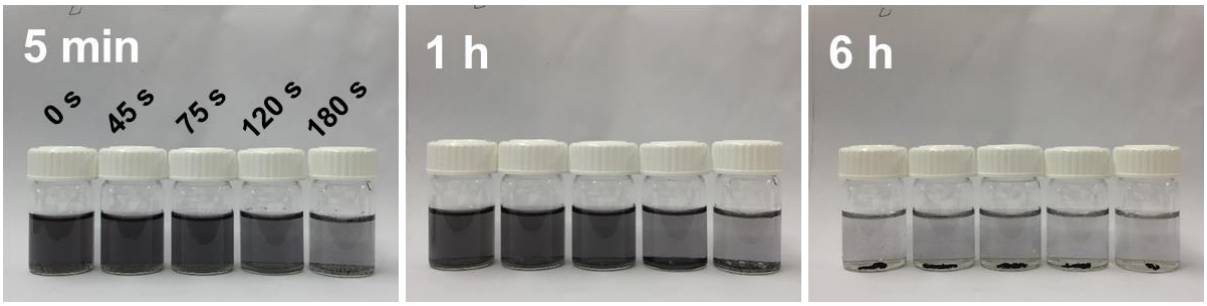

Figure S4. Time-lapse photographs of the gelation of gold NP solutions (triggered by $NaBH_4$) under stirring at 600 rpm for 0, 45, 75, 120, and 180 s.

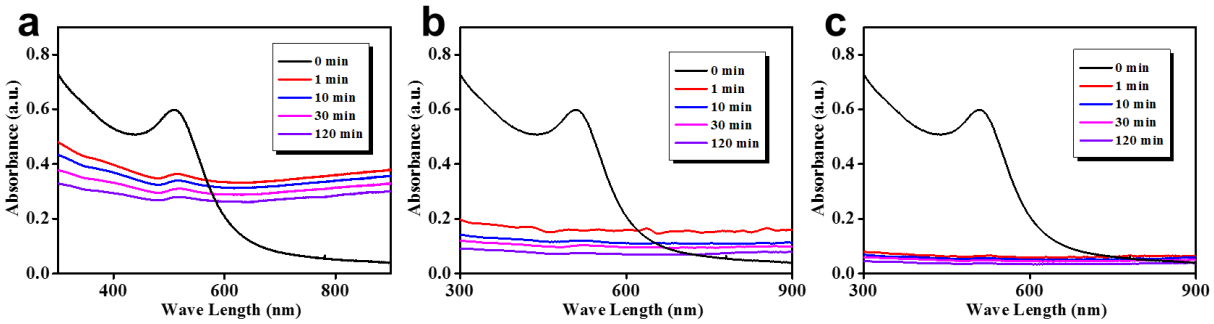

Figure S5. Time-lapse UV-vis spectra of NaCA-stabilized gold NP solutions (c_M = 0.2 mM) after initiation by NH_4F and subsequent stirring for (a) 0 s, (b) 45 s, and (c) 120 s.

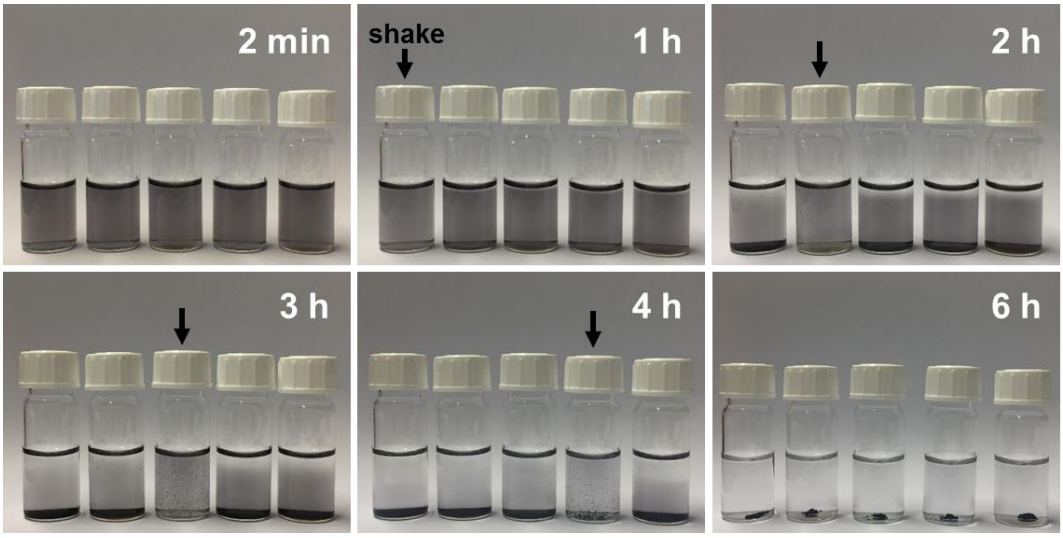

Figure S6. The gelation process of gold NP solutions (triggered by NH_4F) with disturbance introduced at different stages. From left to right vials, the gelation systems were disturbed at 1 h, 2 h, 3 h, 4 h, and without disturbance.

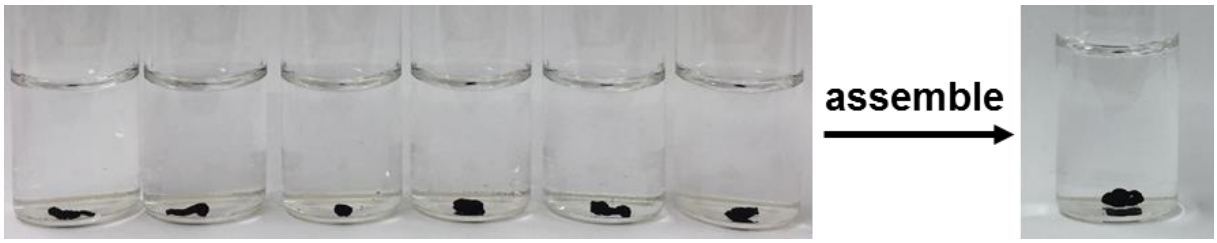

Figure S7. Several as-formed gold hydrogels assemble together into one self-supported hydrogel.

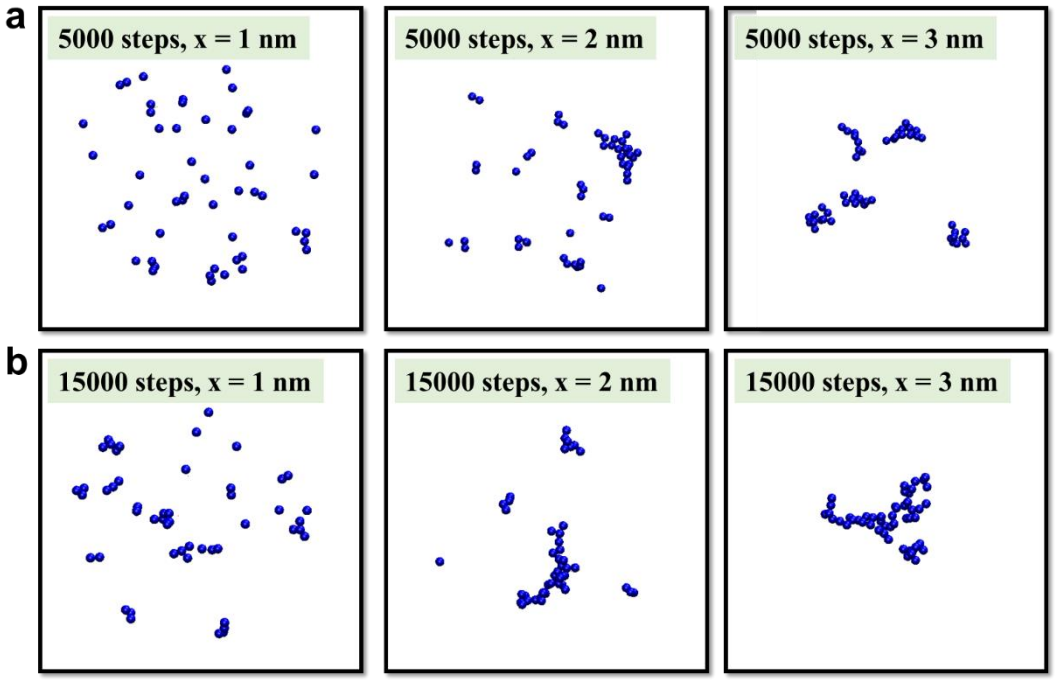

Figure S8. Figures from MC simulations. The aggregation status of particles after (a) 5000 steps and (b)15000 steps with indicated maximum step length x (x=1, 2, 3 nm).

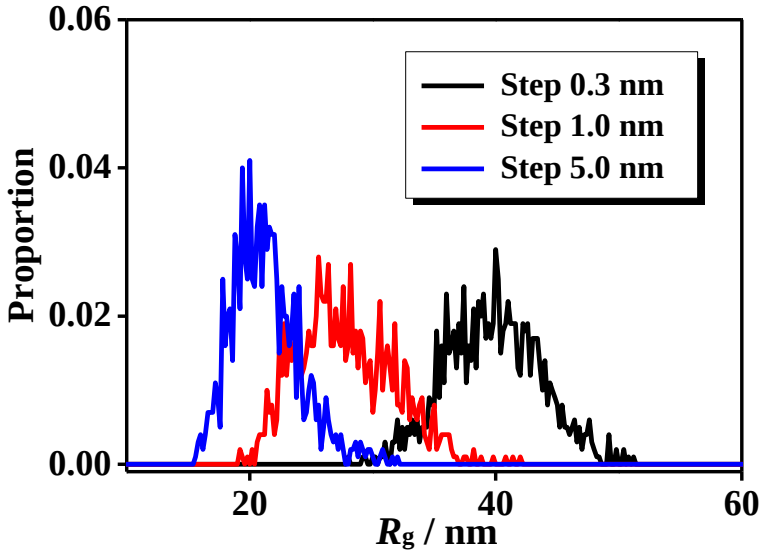

Figure S9. The distribution of the radius of gyration (R_g) of the final single aggregate resulting from MC simulations with different maximum step lengths.

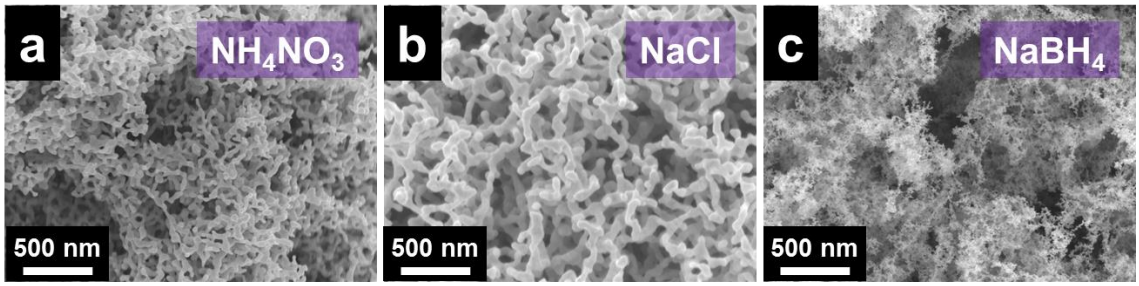

Figure S10. SEM images of stirring-promoted gold gels initiated by different means. Gelation was induced by (a) NH_4NO_3 and (b) NaCl for NaCA-stabilized gold NP solutions, and (c) $NaBH_4$ for PVP-stabilized gold NP solutions.

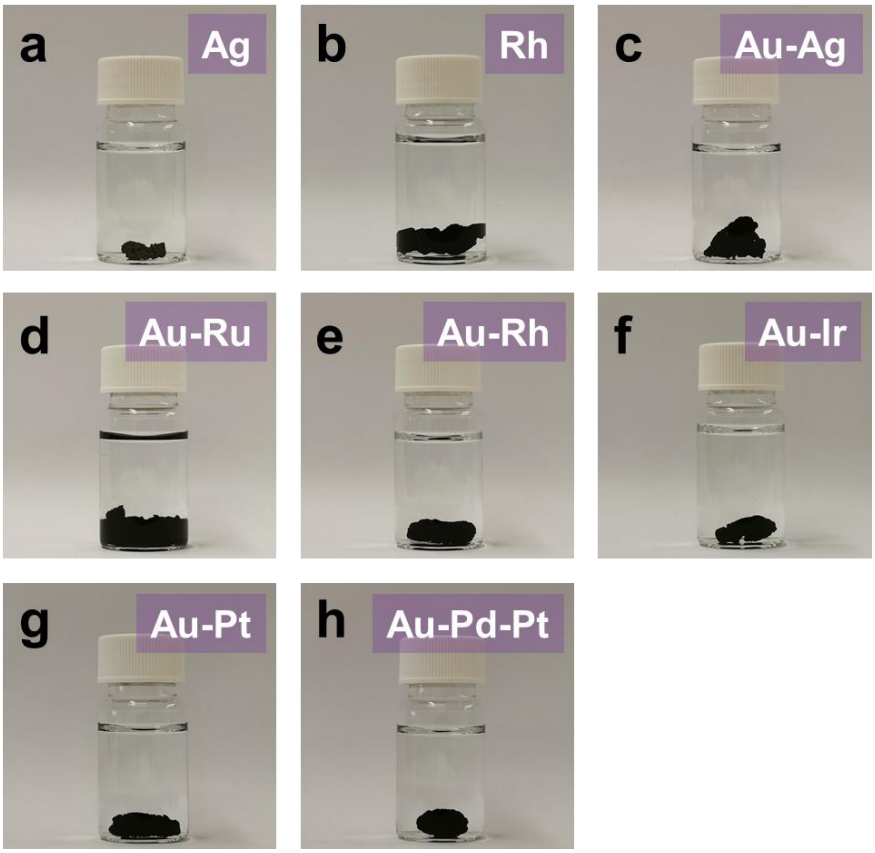

Figure S11. Photographs of noble metal hydrogels with diverse compositions made by the stirring-promoted gelation process initiated by NH_4F.

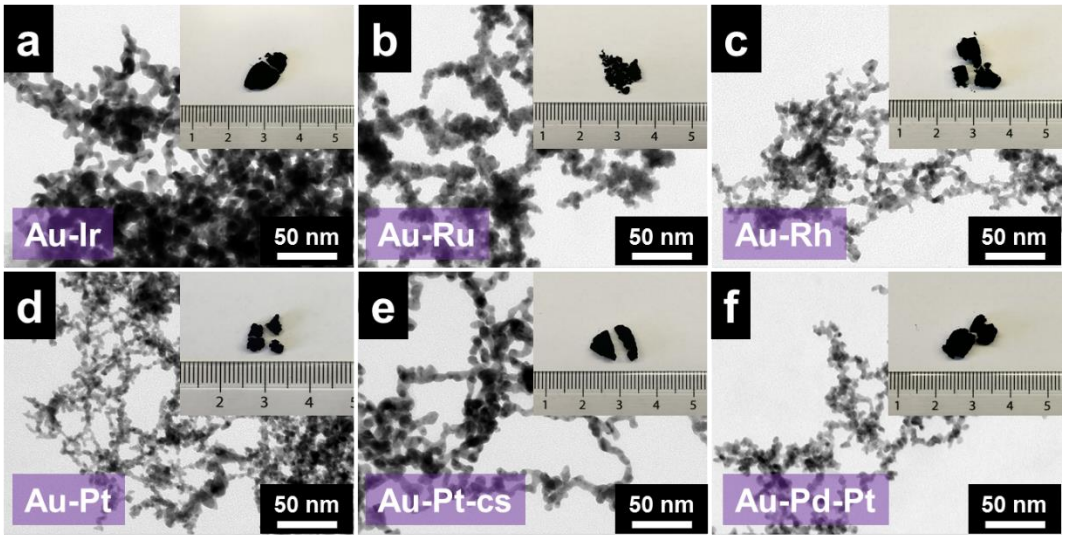

Figure S12. TEM images and photographs (inset) of diverse multimetallic aerogels. Au-Pt-cs indicates the core-shell-structured Au-Pt aerogel.

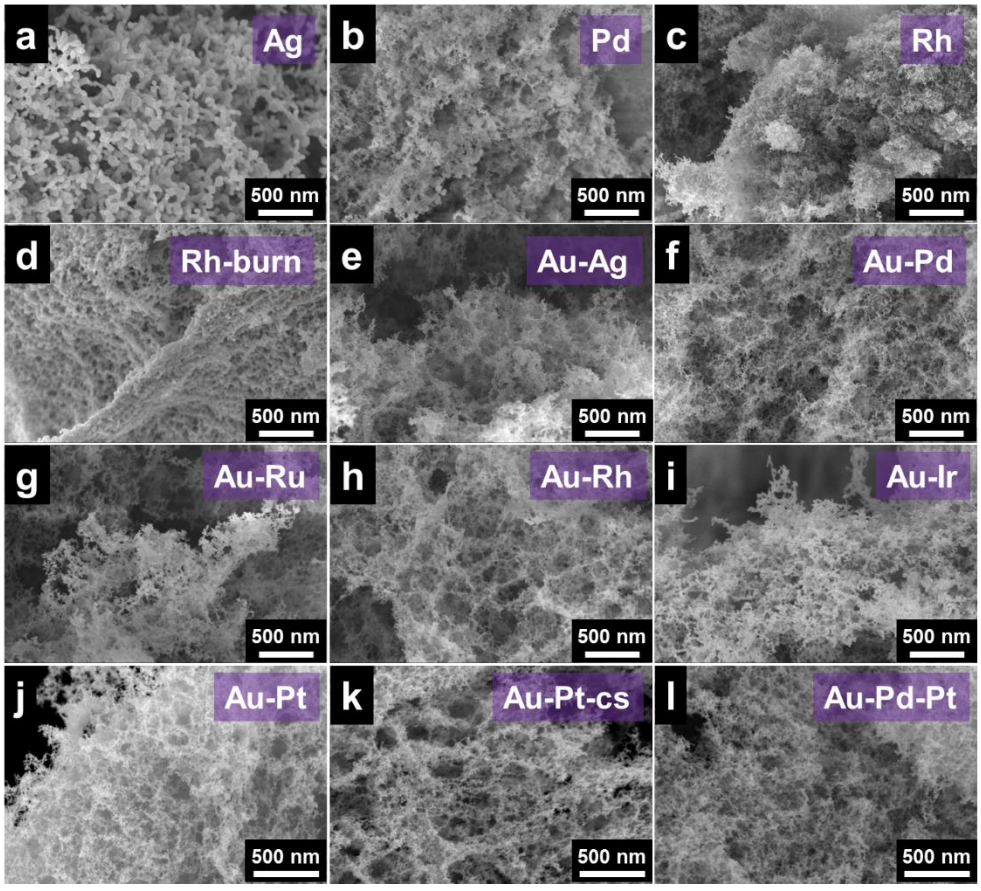

Figure S13. SEM images of noble metal aerogels with diverse compositions. Rh-burn indicates the Rh aerogel after its spontaneous combustion in air.

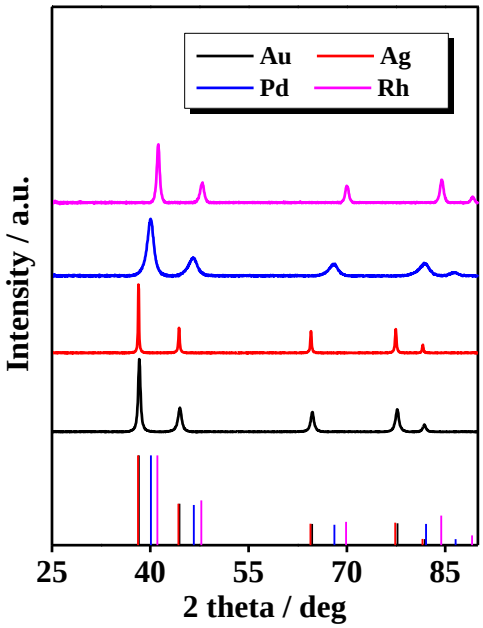

Figure S14. XRD patterns of diverse monometallic aerogels.

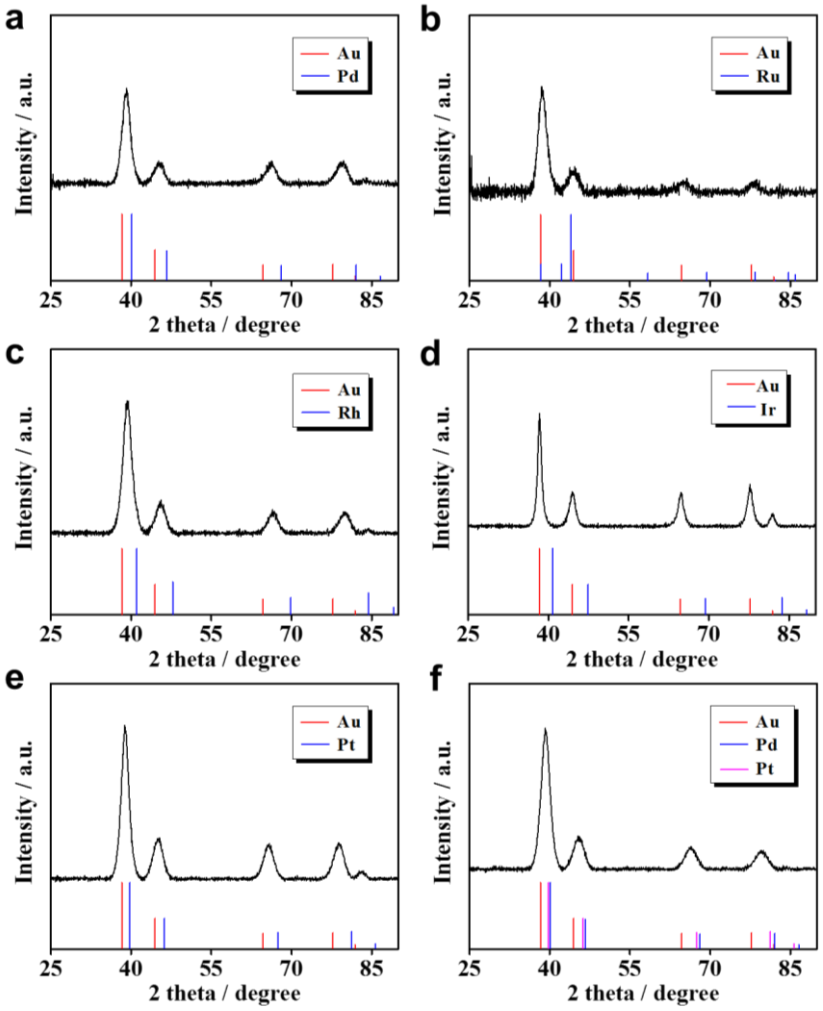

Figure S15. XRD patterns of diverse multimetallic aerogels, (a) Au-Pd, (b) Au-Ru, (c) Au-Rh, (d) Au-Ir, (e) Au-Pt, (f) Au-Pd-Pt.

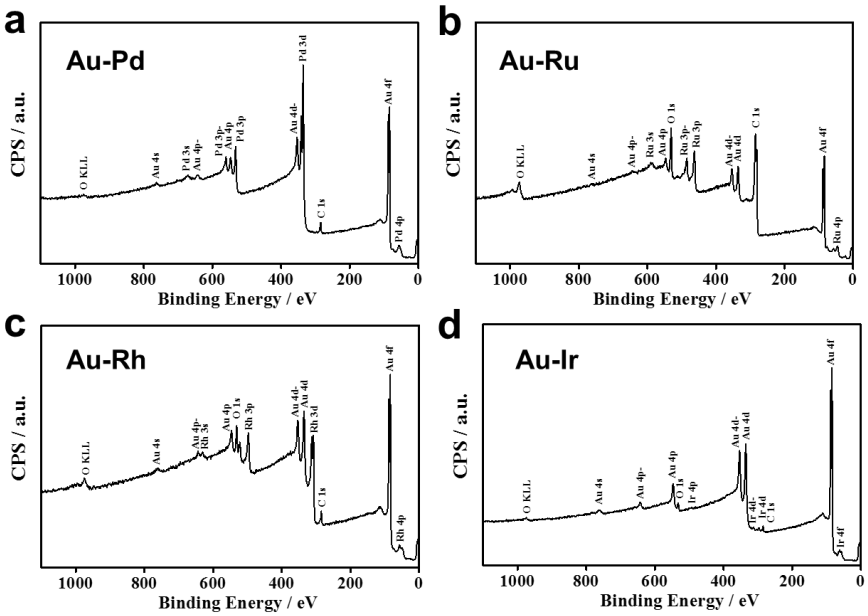

Figure S16. XPS spectra of several bimetallic aerogels, (a) Au-Pd, (b) Au-Ru, (c) Au-Rh, and (d) Au-Ir.

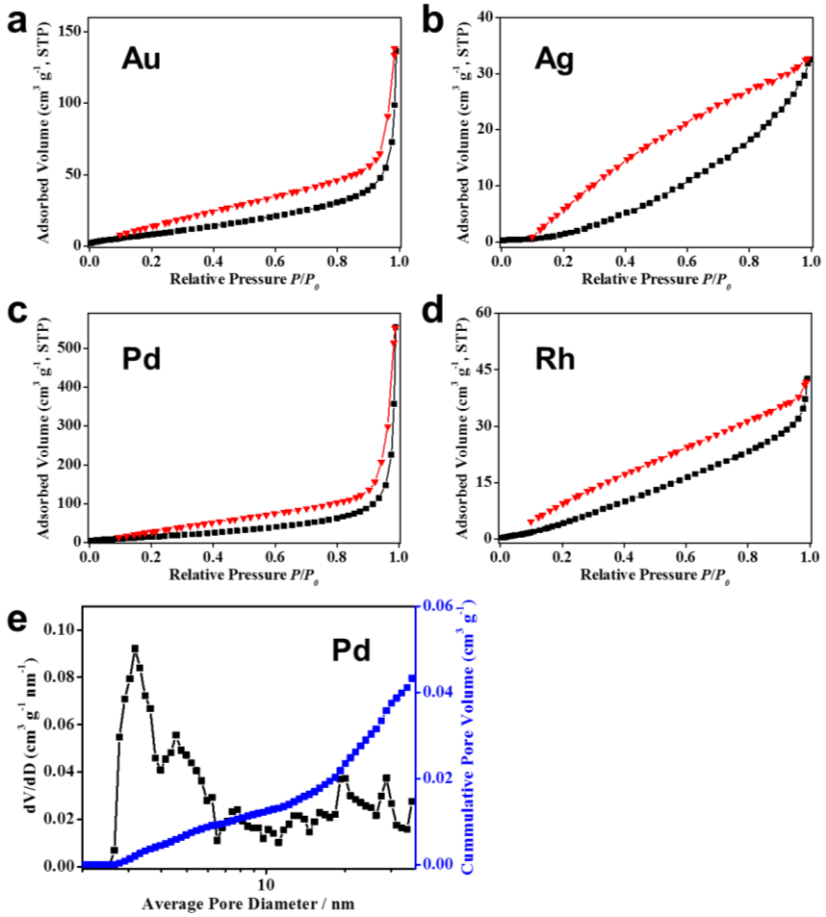

Figure S17. Nitrogen adsorption test of diverse monometallic aerogels. Adsorption/desorption isotherms of (a) Au, (b) Ag, (c) Pd, and (d) Rh aerogels. (e) Pore size distribution of Pd aerogel. The Au gel was fabricated from PVP-stabilized gold NP solution as triggered by $NaBH_4$.

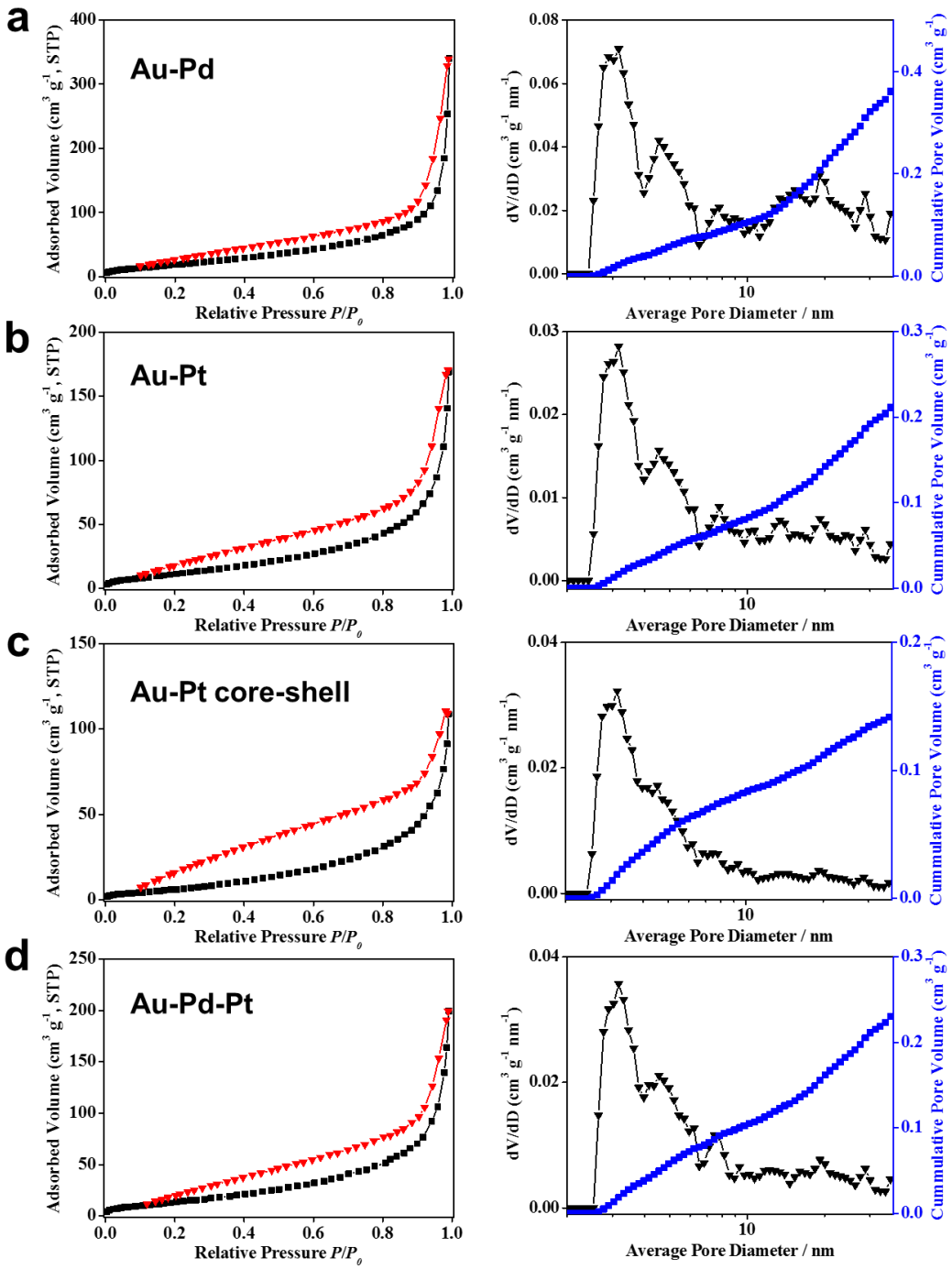

Figure S18. Adsorption/desorption isotherms and pore size distributions of diverse multimetallic aerogels, (a) Au-Pd, (b) Au-Pt, (c) Au-Pt core-shell, and (d) Au-Pd-Pt.

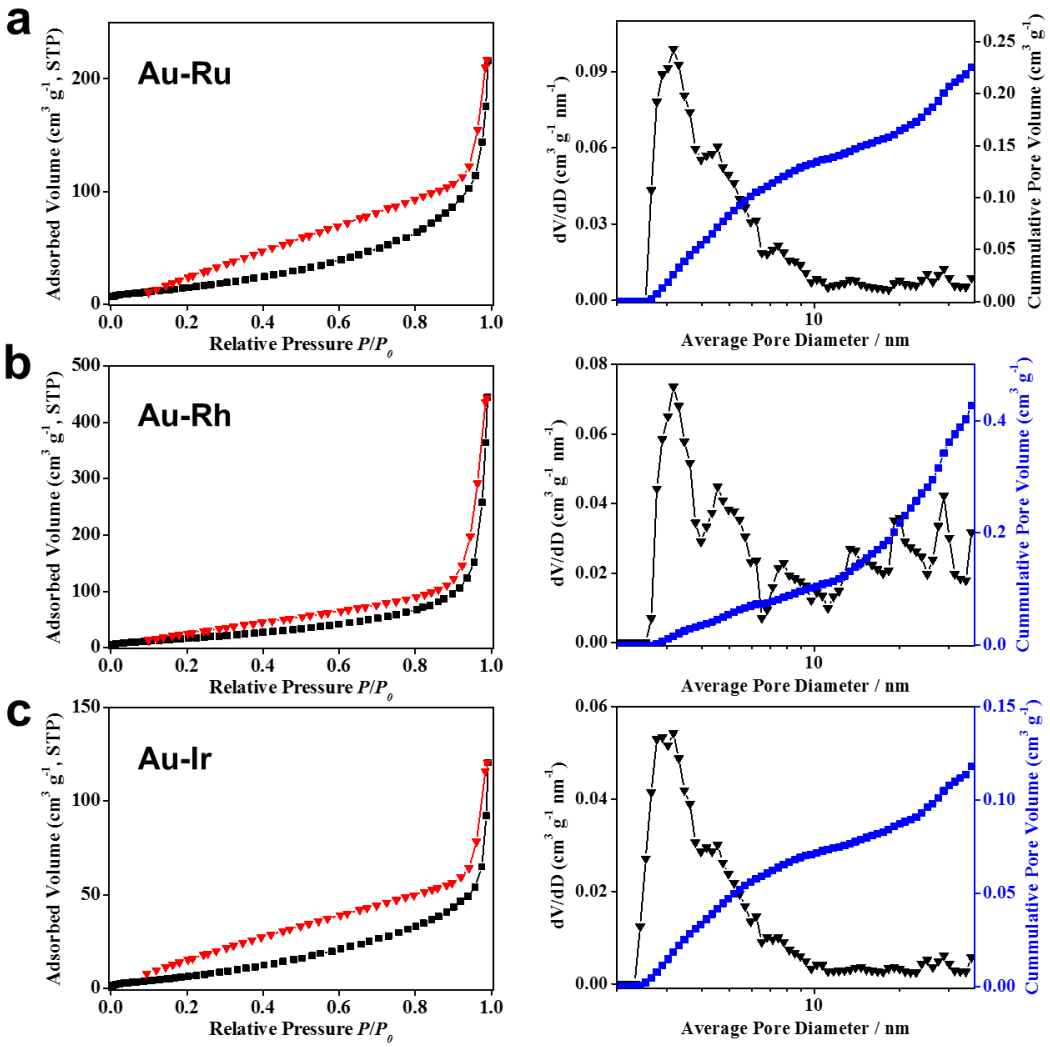

Figure S19. Adsorption/desorption isotherms and pore size distribution of several bimetallic aerogels, (a) Au-Ru, (b) Au-Rh, and (c) Au-Ir.

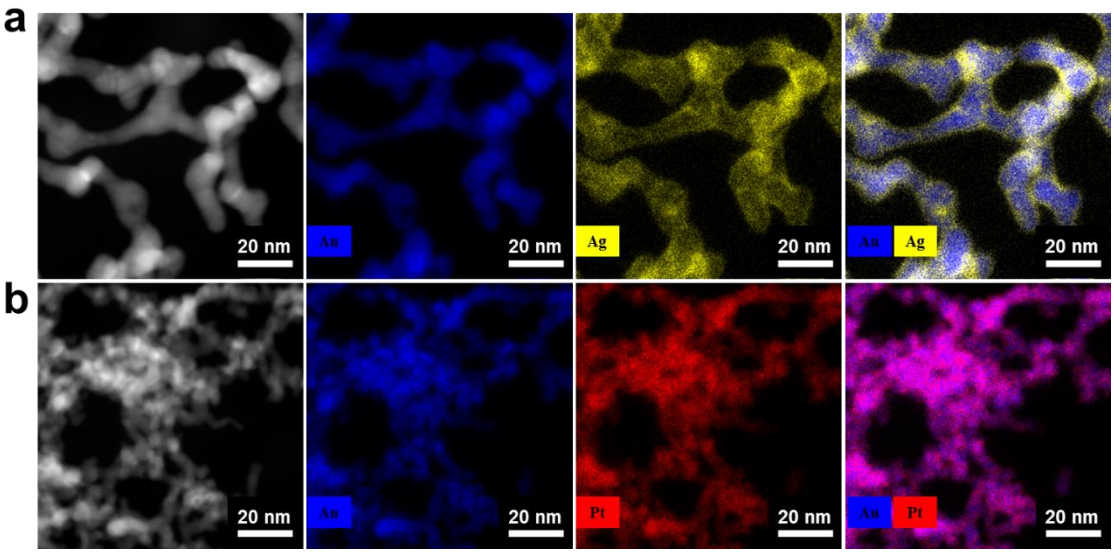

Figure S20. HAADF-STEM imaging and corresponding EDX mapping of multimetallic aerogels, (a) Au-Ag and (b) Au-Pt.

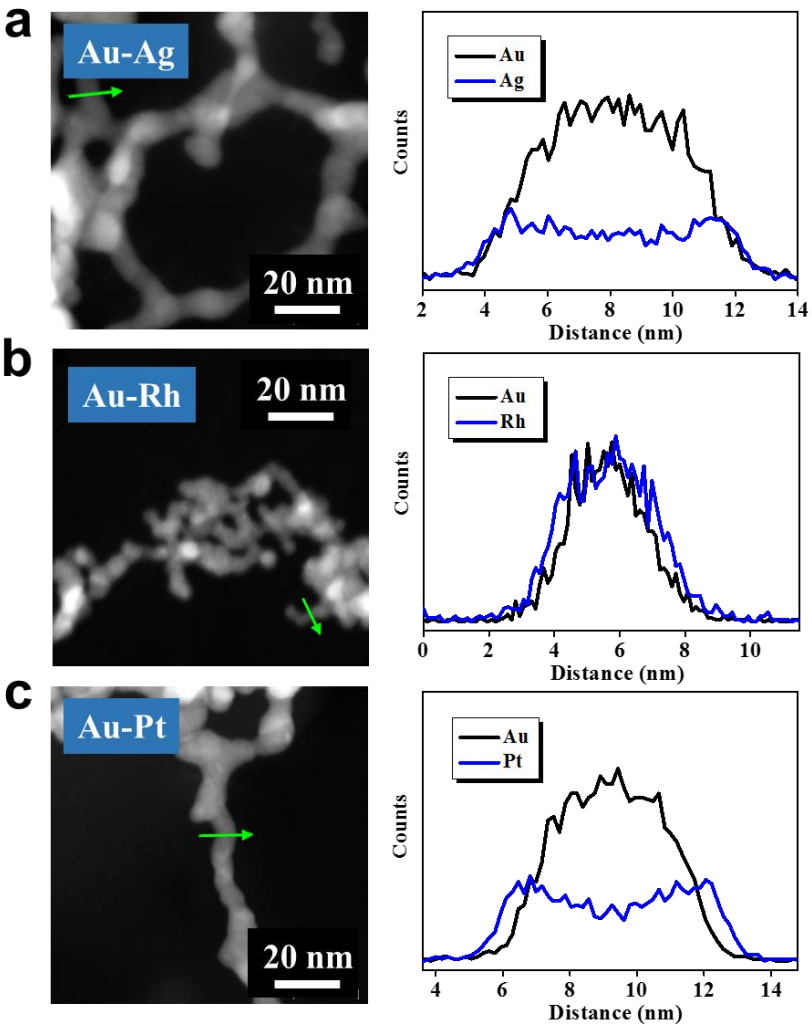

Figure S21. HAADF-STEM imaging and EDX analysis (line scan) of core-shell-structured multimetallic aerogels. The (a) Au-Ag gel and (b) Au-Rh gel were fabricated by directly triggering Au-Ag NP solution with NH_4F. (c) The Au-Pt gel was fabricated by combining the stirring-promoted gelation strategy a dynamic shelling approach.

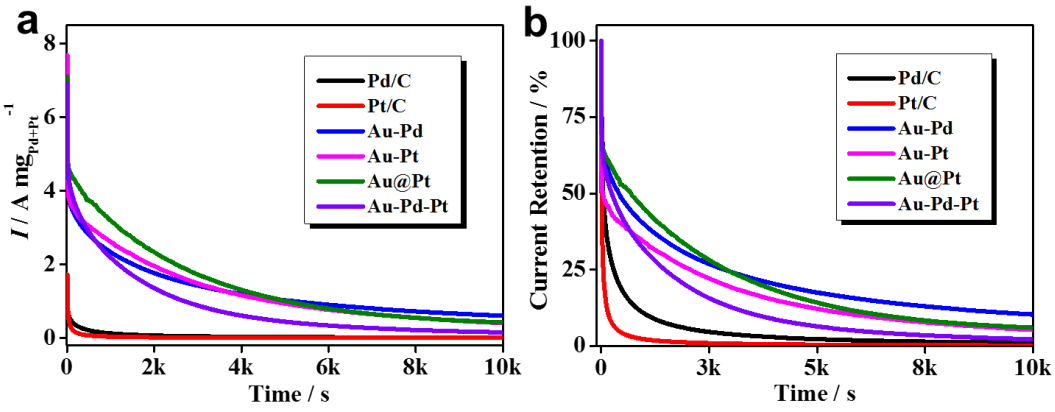

Figure S22. Chronoamperometry tests of various commercial and aerogel electrocatalysts.

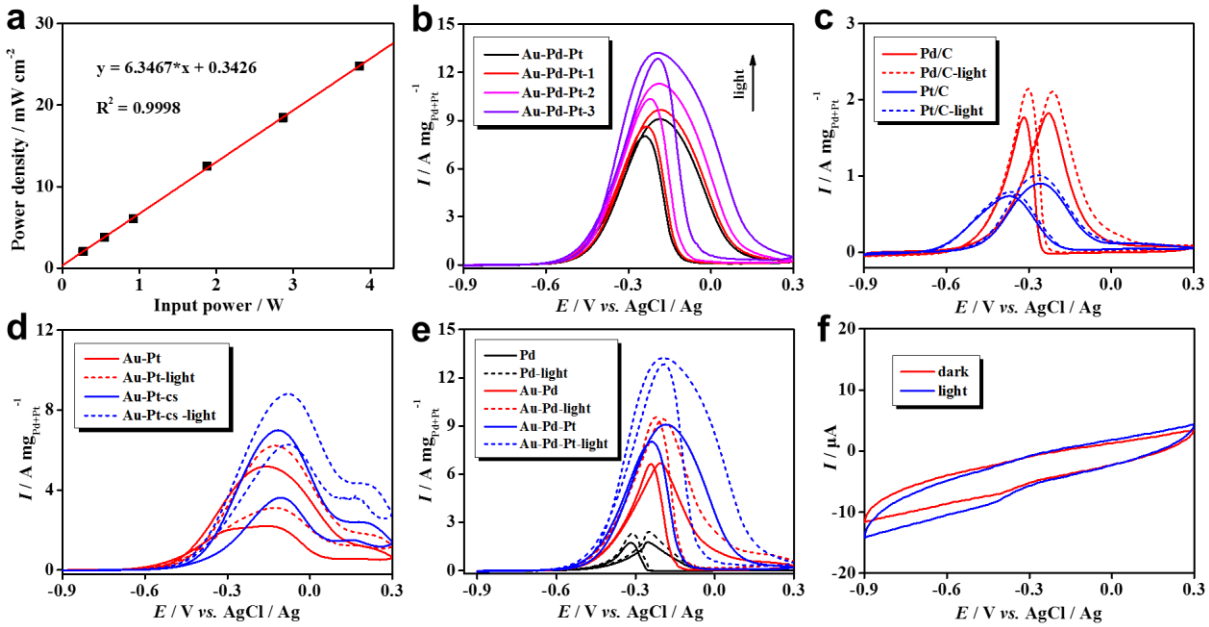

Figure S23. Characterization of the photoelectrocatalytic EOR properties. (a) Linear fitting of the areal light power density of the employed LEDs against the input electrical power. (b) EOR performance of the Au-Pd-Pt aerogel under different light power densities (Au-Pd-Pt denote the dark condition; Au-Pd-Pt-1, 2, 3 denote the light power densities of 12.3, 64.1, and 133.6 mW cm^{-2}, respectively). (c-e) EOR performance of various commercial and aerogel catalysts under dark and light condition (light density of 133.6 mW cm^{-2}). (f) EOR performance on a blank glassy carbon electrode under dark and light condition. All tests were performed in N_2-saturated 1.0 M KOH + 1.0 M ethanol solution at a scan rate of 50 mV s^{-1}.

Tables

Table S1. Comparison of the fabrication conditions of noble metal gels reported in literature.

Metals	Concentrations	Methods	Gelation Time	Ref
Au, Ag, Pd, Rh, Au-Ag, Au-Pd, Au-Pt, Au-Rh, Au-Ru, Au-Ir, Au-Pt core-shell, Au-Pd-Pt	0.02–5.0 mM	Salts or $NaBH_4$ under a disturbing environment	1–10 min	**This work**
Au	0.22 mM	Dopamine	6–72 h	1
Au	0.2 mM	Glucose	~12 h	2
Ag	37.5 mM	$(C(NO_2)_4$	4–12 h	3
Pd	0.8 mM	Glyoxylic acid, sodium carbonate & ~338 K	~1 h	4
Pd	~6.6 mM	In acetic acid, CO & 313 K	5 h	5
Pd	~17 mM	Ca^{2+}	5 min to 2 months	6
Pd	0.2 mM	$NaBH_4$, β-CD	3–10 d	7
Pt	~15 mM	N_2H_4 (in hexane)	1–5 h	8
Au, Pd, Pt	5–100 mM	$NaBH_4$, NaH_2PO_2, or Dimethylamine borane	A few minutes	9
Au, Ag, Pt, Au-Ag, Ag-Pt	10 mM	Ultracentrifugation & H_2O_2	1–4 weeks	10
Au, Ag, Pd, Pt, Au-Ag, Au-Pd, Au-Pt, Pd-Pt, Au-Pd-Pt	0.02–2 mM	Salts	4–48 h	11
Au, Ag, Pd, Pt, Ag–Pd, Ag–Au, Pt–Pd, Ag-Au-Pd	12–24 mM	Hydrazine, 333 K	Several hours	12
AuCu, PdCu, PtCu	0.3 mM	$NaBH_4$, 333 K	6 h	13
Au-Pt	0.6 mM	$NaBH_4$, 333 K	2–4 h	14
Au-Cu	≥ 8 mM	$NaBH_4$	Several minutes	15
Pd-Pt	0.2 mM	$NaBH_4$	3–17 d	16
Pd-Ni	60 mM	Ultracentrifugation, $NaBH_4$, 348 K	< 6 h	17
Pd_xPt_y-Ni	60 mM	Ultracentrifugation, $NaBH_4$, 348 K	< 6 h	18
Pd-Cu	0.3 mM	$NaBH_4$, 333 K	6 h	19
Ir_xCu	1.3 mM	$NaBH_4$, 343 K	2–3 h	20
Au-Ag-Pd	~3 mM	Ultracentrifugation, $(C(NO_2)_4$	16–24 h	21

Table S2. Summary of nitrogen adsorption data and ligament sizes of as-prepared aerogels. The specific surface area S_{BET} (m^2 g^{-1}) was calculated in the partial pressure (p/p_0) range of 0.1–0.3. The total pore volume V_{tot} is derived at p/p_0 =0.99. The average ligament size d is derived from a statistic analysis of TEM measurements.

Entry	Metals	Ligands	Initiators	S_{BET} (m^2 g^{-1})	V_{tot} (cm^3 g^{-1})	d (nm)
1	Au[a]	NaCA	NH_4F	/	/	19.8 ± 3.7
2	Au[a]	PVP	$NaBH_4$	42.6	0.211	10.4 ± 3.1
3	Ag	NaCA	NH_4F	/	/	18.1 ± 3.0
4	Pd	NaCA	NH_4F	76.6	0.857	5.8 ± 1.2
5	Rh[b]	NaCA	NH_4F	38.0	0.245	4.1 ± 0.5
6	Au-Ag[c]	NaCA	NH_4F	/	/	7.1 ± 1.0
6	Au-Pd	NaCA	NH_4F	83.6	0.526	3.9 ± 0.6
7	Au-Pt	NaCA	$NaBH_4$	51.5	0.261	3.7 ± 0.7
8	Au-Pt (core-shell)	NaCA	NH_4F	32.0	0.168	5.3 ± 0.7
9	Au-Rh	NaCA	NH_4F	78.3	0.687	4.6 ± 1.2
10	Au-Ir	NaCA	$NaBH_4$	40.9	0.186	7.2 ± 1.8
11	Au-Pd-Pt	NaCA	NH_4F	60.2	0.309	4.3 ± 0.6

[a] The total concentration of the metal salt precursor was 0.2 mM. For other entries, the concentration was 0.5 mM.

[b] The gel can undergo spontaneous combustion when exposed to air. All parameters were obtained from unburned aerogels.

[c] For the multimetallic systems, the molar ratio of the different metals in the original metal solution is set equally.

References

1. Wen, D., Liu, W., Haubold, D., Zhu, C., Oschatz, M., Holzschuh, M., Wolf, A., Simon, F., Kaskel, S., Eychmüller, A., (2016). Gold Aerogels: Three-Dimensional Assembly of Nanoparticles and Their Use as Electrocatalytic Interfaces. ACS Nano *10*, 2559-2567.

2. Qin, G. W., Liu, J., Balaji, T., Xu, X., Matsunaga, H., Hakuta, Y., Zuo, L., Raveendran, P., (2008). A Facile and Template-Free Method to Prepare Mesoporous Gold Sponge and Its Pore Size Control. J. Phys. Chem. C *112*, 10352-10358.

3. Gao, X., Esteves, R. J., Luong, T. T. H., Jaini, R., Arachchige, I. U., (2014). Oxidation-Induced Self-Assembly of Ag Nanoshells into Transparent and Opaque Ag Hydrogels and Aerogels. J. Am. Chem. Soc. *136*, 7993-8002.

4. Douk, A. S., Saravani, H., Noroozifar, M., (2018). Three-Dimensional Assembly of Building Blocks for the Fabrication of Pd Aerogel as a High Performance Electrocatalyst toward Ethanol Oxidation. Electrochim. Acta *275*, 182-191.

5. Yazdan-Abad, M. Z., Noroozifar, M., Alam, A. R. M., Saravani, H., (2017). Palladium Aerogel as a High-Performance Electrocatalyst for Ethanol Electro-Oxidation in Alkaline Media. J. Mater. Chem. A *5*, 10244-10249.

6. Wen, D., Herrmann, A.-K., Borchardt, L., Simon, F., Liu, W., Kaskel, S., Eychmüller, A., (2014). Controlling the Growth of Palladium Aerogels with High-Performance toward Bioelectrocatalytic Oxidation of Glucose. J. Am. Chem. Soc. *136*, 2727-2730.

7. Liu, W., Herrmann, A. K., Geiger, D., Borchardt, L., Simon, F., Kaskel, S., Gaponik, N., Eychmüller, A., (2012). High-Performance Electrocatalysis on Palladium Aerogels. Angew. Chem. Int. Ed. *51*, 5743-5747.

8. Naskar, S., Freytag, A., Deutsch, J., Wendt, N., Behrens, P., Köckritz, A., Bigall, N. C., (2017). Porous Aerogels from Shape-Controlled Metal Nanoparticles Directly from Nonpolar Colloidal Solution. Chem. Mater. *29*, 9208-9217.

9. Burpo, F. J., Nagelli, E. A., Morris, L. A., McClure, J. P., Ryu, M. Y., Palmer, J. L., (2017). Direct Solution-Based Reduction Synthesis of Au, Pd, and Pt Aerogels. J. Mater. Res. *32*, 4153-4165.

10. Bigall, N. C., Herrmann, A. K., Vogel, M., Rose, M., Simon, P., Carrillo-Cabrera, W., Dorfs, D., Kaskel, S., Gaponik, N., Eychmüller, A., (2009). Hydrogels and Aerogels from Noble Metal Nanoparticles. Angew. Chem. Int. Ed. *48*, 9731-9734.

11. Du, R., Hu, Y., Hübner, R., Joswig, J.-O., Fan, X., Eychmüller, A., (2019). Specific Ion Effects Directed Noble Metal Aerogels: Versatile Manipulation for Electrocatalysis and Beyond. Sci. Adv. *5*, eaaw4590.

12. Tang, S., Vongehr, S., Wang, Y., Cui, J., Wang, X., Meng, X., (2014). Versatile Synthesis of High Surface Area Multi-Metallic Nanosponges Allowing Control over Nanostructure and Alloying for Catalysis and Sers Detection. J. Mater. Chem. A *2*, 3648-3660.

13. Zhu, C., Shi, Q., Fu, S., Song, J., Xia, H., Du, D., Lin, Y., (2016). Efficient Synthesis of MCu (M= Pd, Pt, and Au) Aerogels with Accelerated Gelation Kinetics and Their High Electrocatalytic Activity. Adv. Mater. *28*, 8779-8783.

14. Shi, Q., Zhu, C., Du, D., Bi, C., Xia, H., Feng, S., Engelhard, M. H., Lin, Y., (2017). Kinetically Controlled Synthesis of AuPt Bi-Metallic Aerogels and Their Enhanced Electrocatalytic Performances.

J. Mater. Chem. A *5*, 19626-19631.

15. Wang, J., Chen, F., Jin, Y., Johnston, R. L., (2018). Gold–Copper Aerogels with Intriguing Surface Electronic Modulation as Highly Active and Stable Electrocatalysts for Oxygen Reduction and Borohydride Oxidation. ChemSusChem *11*, 1354-1364.
16. Liu, W., Rodriguez, P., Borchardt, L., Foelske, A., Yuan, J., Herrmann, A. K., Geiger, D., Zheng, Z., Kaskel, S., Gaponik, N., (2013). Bimetallic Aerogels: High-Performance Electrocatalysts for the Oxygen Reduction Reaction. Angew. Chem. Int. Ed. *52*, 9849-9852.
17. Cai, B., Wen, D., Liu, W., Herrmann, A. K., Benad, A., Eychmüller, A., (2015). Function-Led Design of Aerogels: Self-Assembly of Alloyed PdNi Hollow Nanospheres for Efficient Electrocatalysis. Angew. Chem. Int. Ed. *54*, 13101-13105.
18. Cai, B., Dianat, A., Hübner, R., Liu, W., Wen, D., Benad, A., Sonntag, L., Gemming, T., Cuniberti, G., Eychmüller, A., (2017). Multimetallic Hierarchical Aerogels: Shape Engineering of the Building Blocks for Efficient Electrocatalysis. Adv. Mater. *29*, 1605254.
19. Lu, L., Sun, X., Ma, J., Yang, D., Wu, H., Zhang, B., Zhang, J., Han, B., (2018). Highly Efficient Electroreduction of Co2 to Methanol on Palladium–Copper Bimetallic Aerogels. Angew. Chem. Int. Ed. *57*, 14149-14153.
20. Shi, Q., Zhu, C., Zhong, H., Su, D., Li, N., Engelhard, M. H., Xia, H., Zhang, Q., Feng, S., Beckman, S. P., et al., (2018). Nanovoid Incorporated Ir_xCu Metallic Aerogels for Oxygen Evolution Reaction Catalysis. ACS Energy Lett. *3*, 2038-2044.
21. Nahar, L., Farghaly, A. A., Esteves, R. J. A., Arachchige, I. U., (2017). Shape Controlled Synthesis of Au/Ag/Pd Nanoalloys and Their Oxidation-Induced Self-Assembly into Electrocatalytically Active Aerogel Monoliths. Chem. Mater. *29*, 7704-7715.